Structural Optical Magnetodielectric and Antibacterial Properties of Cu Ferrite/ZnO Composite Prepared Via the Sol-gel Ultrasonification Method

Veeramani T¹, Venkataraju C^{1*}, Sathishkumar G²

¹PG & Research Department of Physics, Thiru.Vi.Ka. Government Arts and Science College,
Thiruvarur, Tamilnadu,610003, India.

(Affiliated Bharathidasan University, Thiruchirapalli-620024)

²Department of Physics, Sairam Engineering College, West Tambaram, Chennai – 44, India.
Email: cvrajuphy@gmail.com

The present work reports the structural, optical, magnetodielectric, and antibacterial properties of a system of (1-x) CuFe2O4-ZnO (x=0.0, 0.2, 0.4 and 0.6) composites prepared via the sol-gel ultrasonication technique. The XRD patterns confirmed the presence of tetragonal Cu ferrite and ZnO phases in the composites. XRD analysis indicated that there was a contraction in the crystal structure with increasing ZnO content. The addition of ZnO to the composite increased the energy of the band gap from 1.9 eV to 3.8 eV. The dielectric constant at 1 kHz decreased from 1274 to 107 as the ZnO content in the composite increased. The dielectric constant for all the samples decreases in the presence of an applied magnetic field. Compared with pure CuFe2O4, CuFe2O4 with a ZnO content shows less saturation magnetization and coercivity. Compared with the CuFe2O4 (40 $\mu g/ml$) nanocomposite, the CF0.4/ZnO0.6 (40 $\mu g/ml$) nanocomposite showed better antimicrobial activity. This study may expand the scope of the use of this composite as an electrode material in lithium storage devices and supercapacitors.

Keywords: XRD, nanocomposite.

1. Introduction

Ferrites are magnetic materials that have a spinel structures. The chemical formula for ferrites is MFe₂O₄, where M represents divalent metal cations such as Mn^{2+} , Ni^{2+} , Fe^{2+} , Co^{2+} , Cu^{2+} , and Zn^{2+} [1-4]. Due to their characteristics and diverse applications, ferrites have been the subject of research. Recently, ferrites nanoparticles have drawn a lot of attention due to

their interesting properties, which make them suitable for wide-ranging technological applications. CuFe₂O₄ is a class of ferrite that has received attention from researchers because its structural, electric, and magnetic properties can be tuned by varying environmental conditions. [5-6]. On the basis of the preparation conditions and calcination temperature, CuFe₂O₄ can exist in cubic spinel or tetragonal crystal structures. The photocatalytic activity of CuFe₂O₄ can be enhanced in combination with other photocatalyst materials [7-8]. Chu et al. [9] established that reduced graphene oxide incorporated into copper ferrites (CuFeO₂@rGO and Cu/CuFe₂O₄@rGO) can be used as high-performance electrodes. Nanoparticles of CuFe₂O₄ have potential applications as magnetically recyclable materials for wastewater treatment and as antimicrobial agents. ZnO are a class of group II-IV semiconductors. It has excellent electronic and optical properties. It is also well known for its wide band gap and is widely used because of its nontoxic nature. In recent years, ZnO-based composites have been investigated for possible use as electrode materials in the fields of supercapacitors and lithium-ion batteries [10-12].

However, no studies have been reported for CF/ZnO composites in terms of their magnetodielectric constant or as high-performance electrode materials for supercapacitors and Li-ion storage batteries. The observed variation in the dielectric constant of the CF/ZnO composite upon application of a magnetic field can be utilized to tune the performance of supercapacitors. The present investigation studies the characteristics of ZnO incorporated within a CuFe₂O₄ matrix via a combination of sol-gel and ultrasonic methods. More specifically, we studied its structural, optical, magnetodielectric, and antibacterial properties.

2. Methodology

All the chemicals utilized for the preparation, including Cu (NO₃).6H₂O, Fe (NO₃)₂.9H₂O, ethylene glycol, (Zn (CH₃Co)₂.2H₂O), and KOH, were of analytical grade. CuFe₂O₄ nanoparticles were synthesized via the sol-gel method. Cu (NO₃)6H₂O and Fe (NO₃)9H₂O were dissolved separately in ethylene glycol and mixed well with deionized water. The resulting mixture was maintained at 80°C for a duration of 6 hours to form a dry gel. The dehydrated gel was subsequently subjected to a 5-hour calcination process at 600°C. NPs of zinc oxide were prepared via the sol-gel technique. A solution of zinc acetate at a stoichiometric ratio was prepared with a volume of 100 ml. Next, 100 ml of potassium hydroxide solution with a concentration of 0.2 M was gradually introduced into the mixture while vigorously stirring at 80°C. After vigorous stirring, a white precipitate formed. The resulting white precipitate was then carefully rinsed with distilled water and left to dry in the oven for three hours at 80°C. The dried precipitate was subsequently calcined at 600°C for 5 hrs. The as-prepared CuFe₂O₄ and ZnO nanoparticles were then used to prepare (1-x) CuFe₂O₄+xZnO nanocomposites. Appropriate ratios of the CuFe₂O₄ and ZnO powders were mixed thoroughly and dispersed in distilled water. The resulting solution was then treated with ultrasonication. After vigorous stirring, the solution was filtered and dried at 100°C and calcined at 600°C for 3 hrs.

The antibacterial activity was analyzed via the agar well disc diffusion (Kirby-Bauer) method. Sterile petri plates were dispensed with thirty milliliters of Mueller-Hindon agar medium and allowed to solidify. The plates were then swabbed with the test organism

uniformly via sterile forceps. The discs were then loaded with 10, 20 or 40 μ g/ml samples. Thirty microlitres of standard (chloramphenicol) and 30 μ l of control solution were prepared and placed on the surface of the incubated agar plate. The petri plates were then incubated at 37°C for 24 hours. The antibacterial activity of the samples against the microorganisms was determined by measuring the inhibition zone in mm [13]. The antibacterial effects of both pure copper ferrite and a composite of copper ferrite/zinc oxide on two types of bacteria, E. coli, a gram-negative bacterium, and S. aureus, a gram-positive bacterium, were examined.

Xrd analysis was performed by using an X-ray diffractometer (PAN analytical) to capture the X-ray diffraction patterns of the samples. Optical properties were studied via UV-visible absorption spectroscopy recorded from 200 to 800 nm. The room temperature magnetic measurement was carried out by employing a vibrating sample magnetometer (VSM Quantum Design). The room temperature magnetodielectric measurement of the samples was conducted via LCR HI TESTER (HIOKI 3532-50) equipment across a frequency range of 100 Hz to 1 MHz. An electromagnet was used to apply a magnetic field that varied up to 0.7T.

3. Results and Discussion

XRD AND SURFACE MORPHOLOGY ANALYSIS

The XRD patterns of $CuFe_2O_4$, ZnO and the (1-x) $CuFe_2O_4 + x$ ZnO nanocomposites (x = 0.2, 0.4, 0.6) are shown in Fig. 1. The formation of a phase was evident from the XRD patterns of the tetragonally structured $CuFe_2O_4$ sample (JCPDS card number: 34--0425). From the XRD spectra, peaks corresponding to tetragonally structured $CuFe_2O_4$ are observed at angles of 29.980°, 36.073°, 37.260°, 44.060°, 54.768°, 57.921°, 62.182° and 63.620, which represent planes (112), (103), (211), (202), (220), (312), (321), (224) and (400), respectively. The existence of these planes in the Xrd spectra confirms that the sample of $CuFe_2O_4$ exhibited a tetragonal crystal structure (space group I41/amd). In the present investigation, we obtained a tetragonally structured $CuFe_2O_4$ phase by the sol–gel method, which was calcined at 650°C. Recent studies regarding the phase transition in $CuFe_2O_4$ prepared by the sol–gel method states the formation of a cubic structure after gel calcination, which disappeared at higher temperatures. The phase transition from cubic to tetragonal starts with heat treatment above 400°C [14-15]. The average crystallite size obtained from the Scherrer formula [16].

$$D = \frac{0.9\lambda}{\beta \cos \theta} \tag{1}$$

where β indicates the FWHM. θ represents the peak position, and λ denotes the wavelength of the X-ray. The average crystallite size was calculated, and the values are shown in Table 1. The results revealed a decrease in the crystallite size as the zinc oxide content in the composite increased.

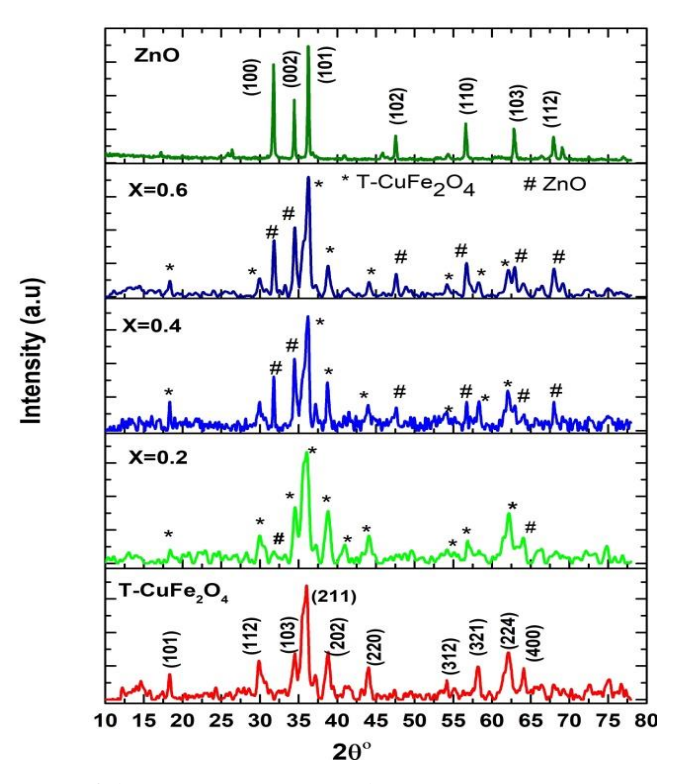


Figure 1. XRD patterns of the $CuFe_2O_4$, ZnO and (1-x) $CuFe_2O_4 + xZnO$ nanocomposites (x = 0.2, 0.4 and x = 0.6).

The lattice parameters "a" and "c" for all the samples were determined from the following equation [16].

$$\frac{1}{d^2} = \frac{h^2}{a^2} + \left(\frac{k^2}{a^2} + \frac{l^2}{c^2}\right) \tag{2}$$

Table 1. Structural parameters for the (1-x) CuFe₂O₄ + xZnO nanocomposite system with different ZnO contents (x=0.0, 0.2, 0.4 and 0.6).

S.No	Sample (x)	Crystallite Size (nm)	Lattice Constant (A°) Ferrite Phase			Lattice Constant (A°) ZnO Phase			Band Gap Energy (Eg)
			a	c	c/a	a	c	c/a	
1	0.0	10.5±1	5.803	8.704	1.5	-	-	-	1.9
2	0.2	15.1±2	5.801	V 8.701	1.5				2.4
3	0.4	14.1±2	5.780	8.669	1.5	3.246	5.186	1.59	3.4
4	0.6	13.1±3	5.773	8.659	1.5	3.245	5.198	1.60	3.8
5	ZnO	23.2±2				3.242	5.192	1.60	

The lattice parameters for the tetragonal copper ferrite are displayed in Table 1. It is evident that there is a contraction in the crystal structure with a rise in the zinc oxide phase, as indicated by the shift in the peak position toward a higher scattering angle. The lattice parameter "a" decreased from 5.803 to 5.773, and "c" decreased from 8.704 to 8.659. The

characteristic peaks appearing at 31.768°, 34.438°, 36.260°, 47.538°, 56.595°, 62.856° and 67.953°, represent the planes (100), (002), (101), (102), (110), (103) and (112), respectively. The angular positions of the XRD peaks of the ZnO phase shift with increasing ZnO content in the composite. The lattice parameters "a" and "c" can be calculated from the following relation [17].

$$\frac{1}{d^2} = \frac{4}{3} \left(\frac{h^2 + k^2 + l^2}{\alpha^2} + \frac{l^2}{c^2} \right) \tag{3}$$

It is evident from the Table 1. There is substantial change in the lattice parameters of ZnO in the composite. The lattice parameter "a" increased from 3.242 to 3.246, and "c" decreased from 5.192 to 5.186. This difference in the lattice parameter may be due to the presence of the $CuFe_2O_4$ phase in the composite.

SEM images of all the samples (1-x) containing CuFe2O4+xZnO (x= 0.0, 0.2, 0.4, 0.6) are displayed in Figure 2. (a-d). It is evident that the particles are less agglomerated and uniformly distributed in pure CuFe₂O₄. The incorporation of ZnO nanoparticles into the CuFe₂O₄ ferrite matrix resulted in the uniform distribution of smaller particles along with larger particles.

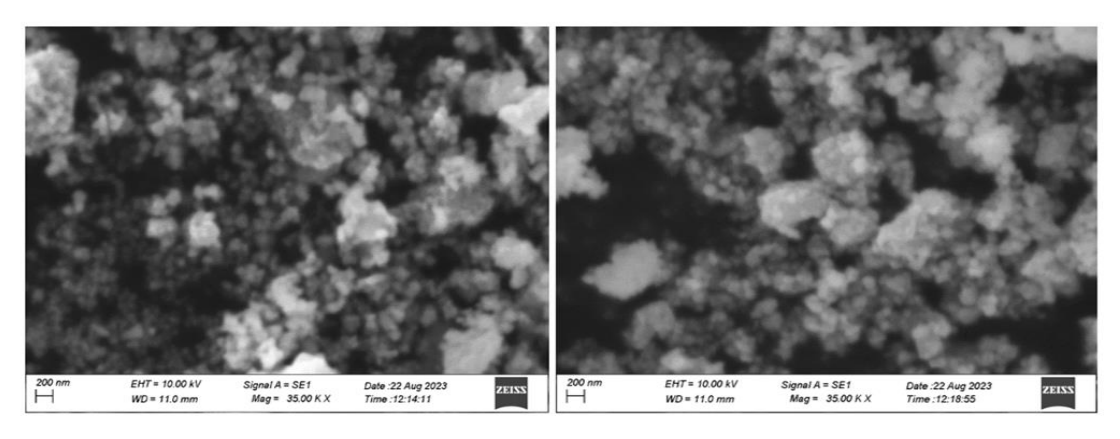


Figure 2. SEM micrographs of the (1-x) $CuFe_2O_4 + xZnO$ nanocomposites: (a) x = 0.0 and (b) x = 0.4.

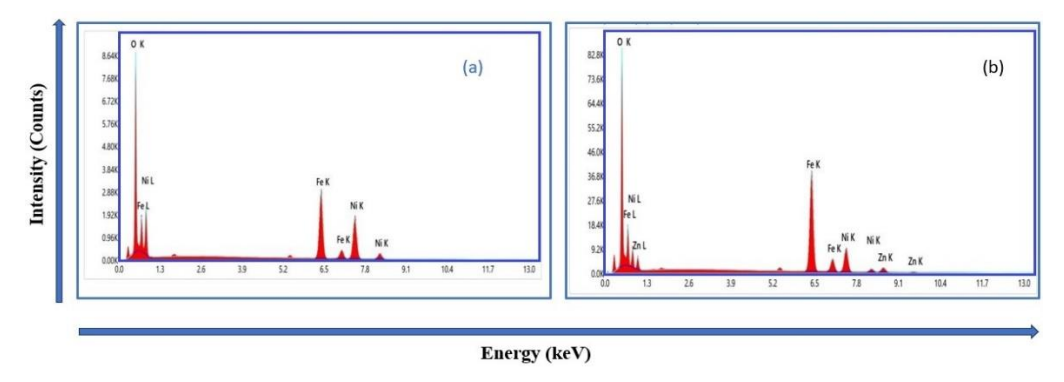


Figure 3. SEM micrographs of the (1-x) $CuFe_2O_4+xZnO$ composites: (a) x=0.0 and (b) x=0.30

Nanotechnology Perceptions Vol. 20 No.6 (2024)

UV studies

Figure 3 displays the UV–Vis absorption spectra plotted in 300-500 nm wavelength range. The absorption peak at 394 nm displays the characteristic peak for the sample of CuFe₂O₄. The absorption peak for ZnO reported in the literature is at 420 nm [18]. The absorption peak for the (1-x) CuFe₂O₄-xZnO nanocomposite (x=0.2, x=0.4 and x=0.6) appears to shift from 396.2 nm to 398 nm relative to that of pure CuFe₂O₄.

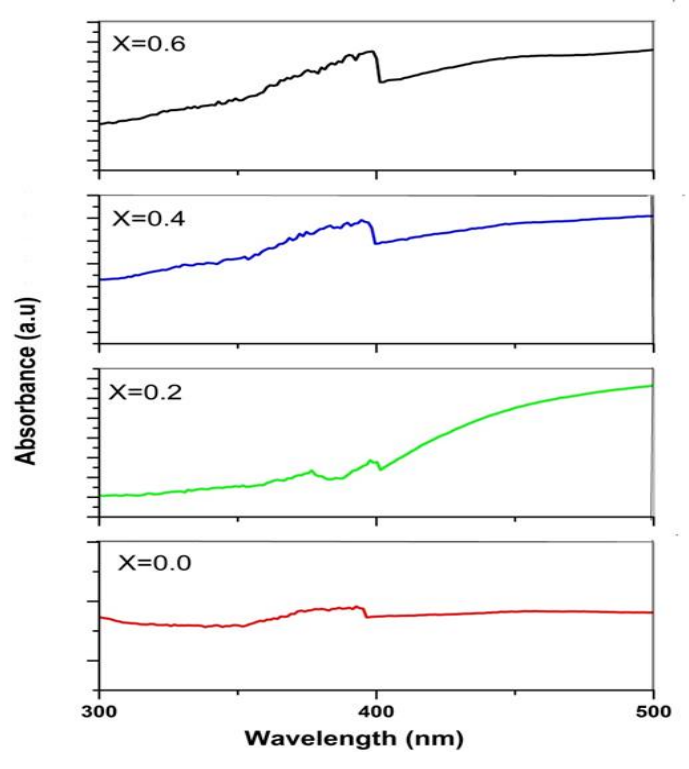


Figure 3. UV spectra of the system (1-x) $CuFe_2O_4 + xZnO$ nanocomposites (x = 0.0, 0.2, 0.4 and 0.6).

The addition of ZnO to the ferrite matrix clearly widened the absorption range. The appearance of the absorption peak is reportedly due to the transition of electrons occurring between valence band and the conduction band [19]. The shift in the peak position with increasing ZnO content in the sample may be due to the variation in the bandgap. The Tauc relation [18] can be employed to find the band gap values for all the samples.

$$\alpha h \nu = A(\alpha h \upsilon - E_g)^n \tag{4}$$

where α indicates the absorption constant, hv is the photon energy, E_g is the band gap energy, "A" is the constant, "n" is ½ for the direct band gap and "n" is 2 for the indirect band gap [18].

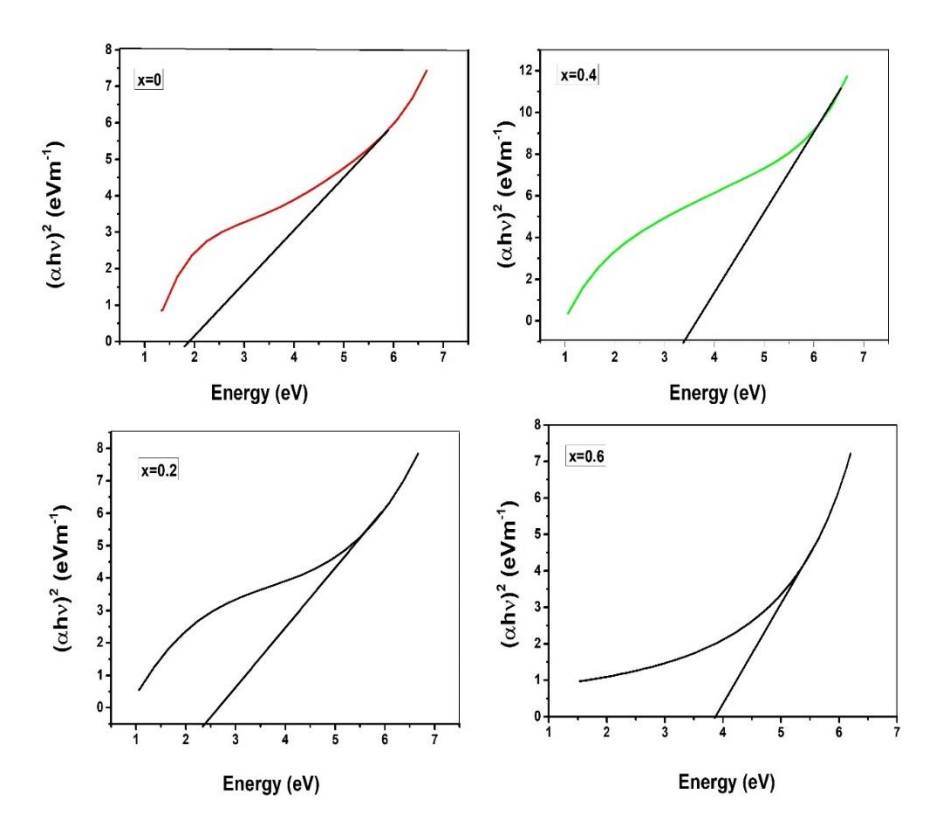


Figure 4. Tauc plots for the (1-x) $CuFe_2O_4 + xZnO$ nanocomposites (x = 0.0, 0.2, 0.4 and 0.6).

Figure 4 displays the Tauc plot for all the samples. By extrapolating the curve to zero on the x-axis, the energy band gap (Eg) for all the samples can be obtained. The values of the band gap energy are displayed in Table 1. The low band gap value of Ni ferrite is improved from 1.9 eV to 3.8 eV when a higher band gap material such as ZnO is used. As a result of structural changes with increasing ZnO content, the energy level between the valance band and the conduction band increases, leading to an increase in the band gap. [20].

VSM studies

Figure 5 shows the room temperature magnetization curve for the system $(1-x)(NiFe_2O_4) + x(ZnO)$ (with x=0.0, 0.2, 0.4, 0.6). The hysteresis loop for all the samples is found to exhibit a ferromagnetic nature. The calculated values of all the magnetic parameters for the samples are shown in Table 2.

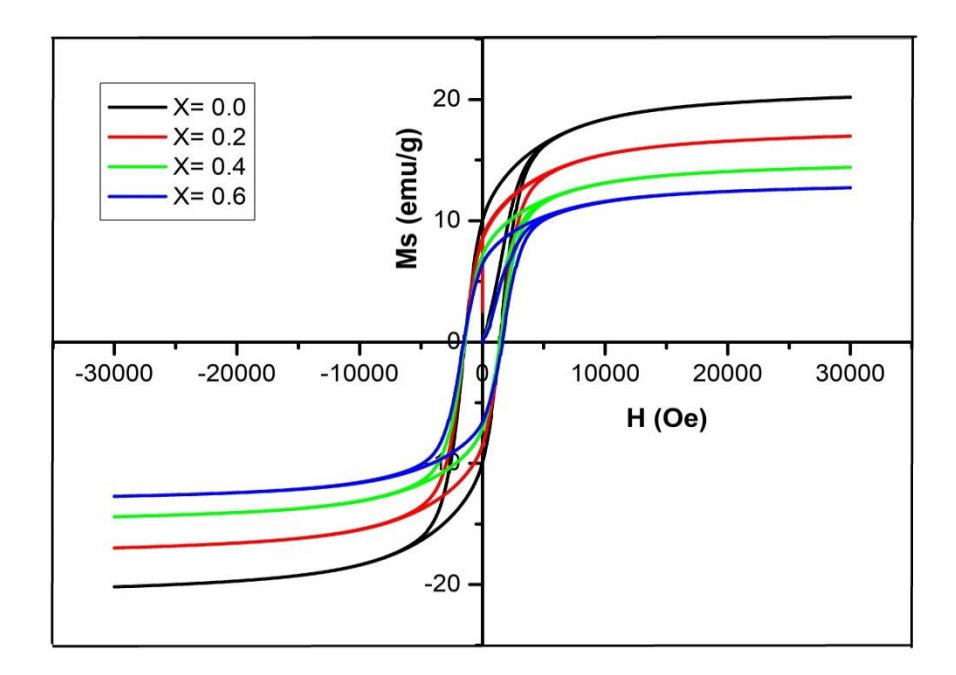


Figure 5. Magnetization hysteresis loops for the (1-x) CuFe₂O₄ + xZnO system (x = 0.0, 0.2, 0.4 and 0.6).

The saturation magnetization for all the samples gradually increases and reaches a maximum for a field greater than 30000 Oe. The saturation magnetization decreases from 20.2 emu/gm to 12.3 emu/gm with increasing ZnO content. In the present study, we obtained a saturation magnetization value of 20.2 emu/gms. A saturation magnetization value of 30.9 emu/gms for the CuFe₂O₄ prepared via the sol-gel method at 300°C have been reported by L. Khanna et al. [21]. R. S Yadav et al. reported a saturation magnetization value of 17.6 emu/gms for copper ferrite synthesized via the sol-gel autocombustion method and then calcined at 800°C [22]. Ravi Kumar et al. [23] obtained a saturation magnetization value of 35.8 emu/gms for CuFe₂O₄ synthesized via the sol-gel method and calcined at 1000°C. The magnetic parameters of ferrite nanoparticles depend on many factors, such as crystallinity, particle size, method of synthesis, sintering process and exchange interaction [24-25]. This variation in the saturation magnetization of CuFe₂O₄ may be due to these factors. The distribution of Cu²⁺ ions and Fe²⁺ ions among tetrahedral and octahedral sites also influences the net magnetic moment. The decrease in the saturation magnetization of the CuFe₂O₄ nanoparticles with increasing ZnO content may be due to the presence of nonmagnetic ZnO nanoparticles in the ferrite matrix. Notably, the coercivity of the tetragonal CuFe₂O₄ nanoparticles is greater than that of the cubic $CuFe_2O_4$ particles. The remanence ratio M_r/M_s , also known as the squareness ratio in the current investigation, was found to rise with increasing ZnO content. The squareness value of approximately 0.5 for all the samples indicate single-domain ferrimagnetic particles [24].

S.No	Sample (x)	M _s (emu/gms)	H _c (Oe)	H _r (emu/gms)	M _r /M _s	K x 10 ³ (emu.Oe g ⁻¹)
1	0.0	20.2	1332	9.9	0.49	28.1
2	0.2	17.1	1366	9.6	0.56	24.3
3	0.4	14.2	1379	8.1	0.57	20.4
4	0.6	12.3	1398	7.2	0.58	17.9

Table 2. Magnetic parameters of the CuFe₂O₄ system with different ZnO contents (x=0.0,0.2, 0.4 and 0.6)

The anisotropy constant is determined from the following relation.

$$Hc = \frac{0.96 \text{ K}}{M_{\odot}} \tag{5}$$

where K represents the anisotropy constant. The magnetocrystalline anisotropy is a magnetic parameter used to refer to the reorientation of the directions of magnetic moments toward their preferred easy axis when the field is switched off [22]. The major cause of magnetocrystalline anisotropy is spin–orbit interactions. The strong spin-orbit interaction between the Cu²⁺ ions and the Fe³⁺ ions contributed to the magneto-crystalline anisotropy in the copper ferrites. The calculated values of the anisotropy constant K are tabulated in Table 2 and are found to decrease with increasing ZnO content.

Magnetodielectric studies

The magnetodielectric constant for the system of (1-x) CuFe₂O₄ + xZnO (x = 0.0, 0.2 and 0.4) measured at room temperature under different magnetic fields is depicted in Figure 6(a-d). All the samples clearly displayed dielectric dispersion, and the dielectric constant decreased with increasing frequency. This higher and lower value of the dielectric constant can be understood on the basis of the space charge polarization model. According to Maxwell–Wagner theory, the resistance at the grain boundary tends to accumulate electrons at the boundary, leading to an increase in polarization [26]. At higher frequencies, the electrons cannot follow the a.c. field, and as a result, the number of electrons reaching the grain boundary decreases. As a consequence of this effect, the net dielectric constant decreases with frequency. In ferrites, the polarization mechanism is comparable to that of the conduction mechanism. The exchange of electrons between Fe²⁺ and Fe³⁺ induces polarization. At higher frequencies, the exchange cannot follow the a.c. field and hence becomes constant.

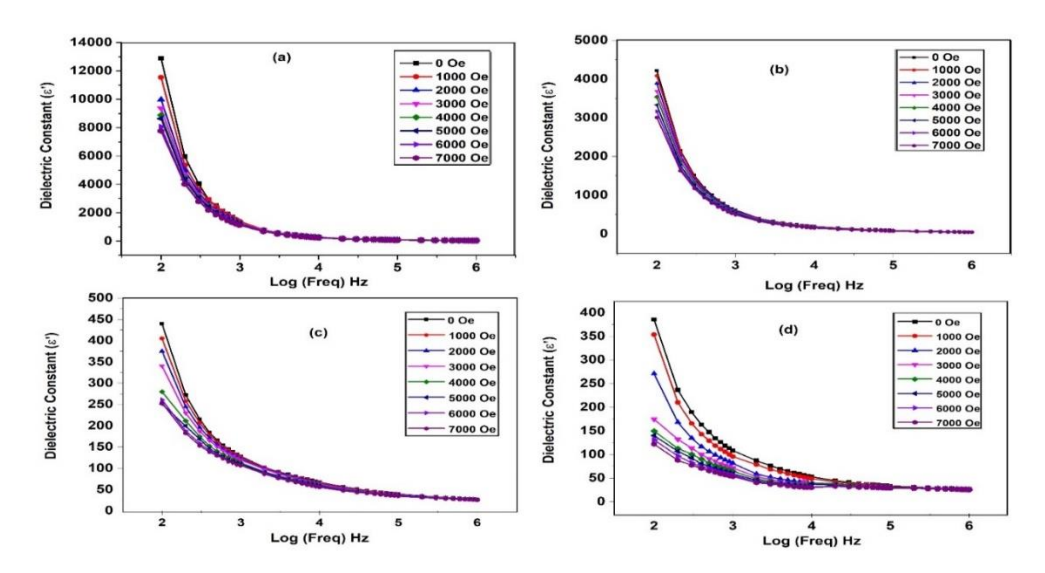
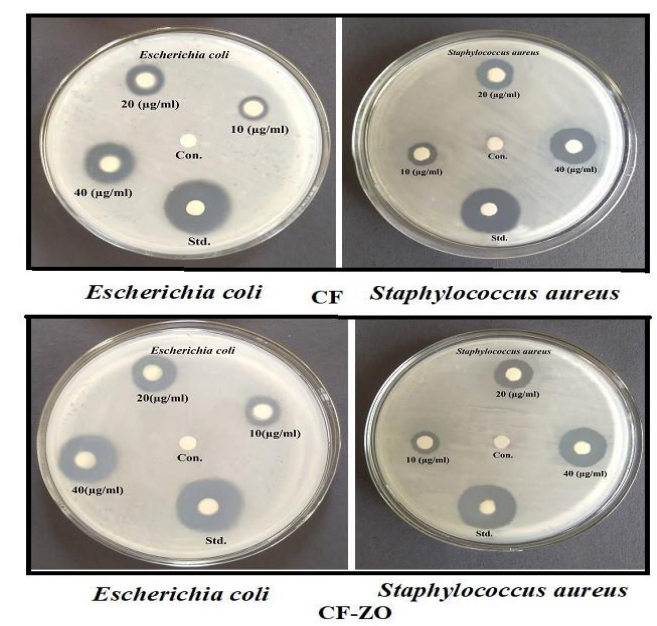


Figure 6. Dependence of ε' on log (Freq) under a magnetic field for the (1-x) CuFe₂O₄ + xZnO system.(a). (x=0.0), (b). (x=0.2), (c). (x=0.4) and (d) x=0.6 with a magnetic field.

The dielectric constant for tetragonal copper ferrite in the present study is 1274, as measured at 1 kHz. Faten Haithum Mulud et al. measured a dielectric constant value of approximately 2500 for copper ferrite prepared via the sol-gel method [27]. The value of the dielectric constant for the (1-x) $CuFe_2O_{4-x}ZnO$ nanocomposite (x=0.0, x=0.2, x=0.4 and x=0.6) lies in the range of 1274 to 107 measured at 1 kHz without a magnetic field. The decrease in the dielectric constant with increasing ZnO content may be due to the change in space charge polarization as a result of variations in the grain boundary resistance. All the samples show a decrease in the dielectric constant in response to the magnetic field. The current investigation of the dielectric constant for copper ferrite (x=0.0) measured at 1 kHz in the absence of a magnetic field revealed a value of 1274, which decreased to 1118 at a field of 7000 Oe. The dielectric constant measured for the sample x = 0.6 at 1 kHz varied from 107 to 53 for a field of 7000 Oe. The other reasons reported in the literature for changes in the dielectric constant are the grain size, grain boundaries, cation distribution and structural distortion [28].

Antibacterial studies

The antimicrobial effects of the $CuFe_2O_4$ and $CuFe_2O_4/ZnO$ nanocomposites were explored against gram-positive bacteria (Staphylococcus aureus) and Escherichia coli (gram-negative bacteria) at various concentrations via the disc diffusion method. The antibacterial effects of the $CuFe_2O_4$ and $CuFe_2O_4/NiO$ nanocomposites on the zone of inhibition that appeared on the agar plate were investigated. Table 3 displays the diameter of inhibition measured in mm. Figure 7 shows the outcome of the antibacterial actions as an area of inhibition. Figure 8 shows a bar diagram of the antibacterial actions in the form of an area of inhibition. As the concentration of the $CuFe_2O_4$ and $CuFe_2O_4/ZnO$ nanocomposite loading increased, the antibacterial effect on the bacteria Escherichia coli and Staphylococcus aureus increased, as evidenced by an increase in the inhibition diameter on the agar plate.



CF-ZO

Figure 7. Antibacterial activity of copper ferrite and copper ferrite/zinc oxide nanocomposites on Escherichia coli and Staphylococcus aureus.

Table 3. Zone of inhibition (mm) of the CuFe₂0₄ and CuFe₂0₄/ZnO composites.

Sample	Microbial strains	Sample dose	Std.	(30 µl)			
		10 μg/ml	20 μg/ml	$40 \mu g/ml$			
		Zone of inhibitions mm					
	Escherichia coli	5.30±0.03	11.30±0.07	14.00±0.09	14.55±	14.55±0.101	
CuFe ₂ O ₄	Staphylococcus aureus	4.75±0.03	11.00±0.09	13.70±0.09	3.70±0.09 14.30±0.		
	Escherichia coli	5.50±0.03	11.50±0.08	8 14.15±0.09		14.90±0.10	
CuFe ₂ O ₄ /ZnO	Staphylococcus aureus	4.90±0.03	11.10±0.09	13.85±0.09	14.35±	0.10	

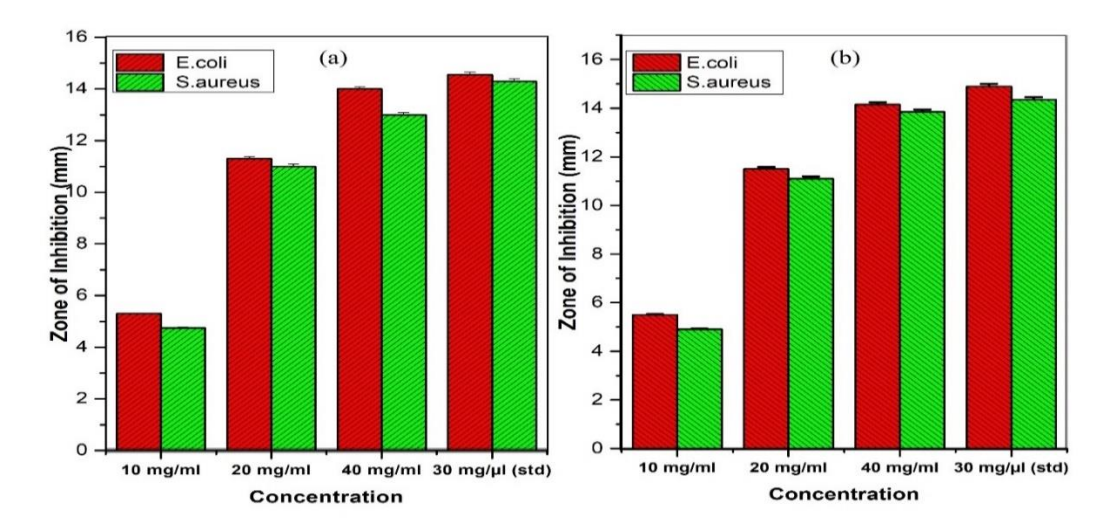


Figure 8. Bar diagram of the antibacterial activity of copper ferrite and copper ferrite/Zinc Oxide nano composite on Escherichia coli and Staphylococcus aureus.

The results of the investigation indicate that, compared with pure $CuFe_2O_4$, the $CuFe_2O_4$ /ZnO nanocomposite had better antibacterial activity at a concentration of 40 µg/ml, with inhibition diameters of 14.15 mm for Escherichia coli and 13.85 mm for Staphylococcus aureus. The interaction of nanoparticles around the cell walls of bacteria is a type of mechanism that has been reported in the literature for antibacterial action against pathogens [29]. Owing to electrostatic interactions with the cell wall, the metal ions present on the surface of the nanoparticles penetrate the cell by destroying the cell membrane and causing cell death. This antibacterial property of $CuFe_2O_4/ZnO$ can be used as a disinfectant in water bodies.

4. Conclusion

CuFe₂O₄/ZnO composites were prepared via the sol–gel ultrasonication method. A variation in the lattice parameter for the tetragonally structured CuFe₂O₄ was observed with increasing zinc oxide content. The addition of ZnO improved the light-absorbing range and the band gap value in CuFe₂O₄. The dielectric constant for all the samples decreased with increasing magnetic field. The coercivity and remanent ratio are found to increase with increasing ZnO content. CuFe₂O₄/ZnO (40µg/ml) composite showed better antibacterial activity with inhibition diameter of 14.40 mm for E. coli and 14.30 mm for S. aureus compared to pure CuFe₂O₄ (40µg/ml). Thus, the results of this investigation reveal that the CF/ZnO composite has potential for application in lithium storage devices and supercapacitors as an electrode material.

References

- [1]. M.P. Ghosh, S. Datta, R. Sharma, K. Tanbir, M. Kar, S. Mukherjee, Mater. Sci. Eng., B 263, 114864, (2021). https://doi.org/10.1016/j.mseb.2020.114864.
- [2]. M. Rashad, D. Rayan, A. Turky, M. Hessien, J. Magn. Magn Mater. 374, 359–366, (2015). https://doi.org/10.1016/j.jmmm.2014.08.031.
- [3]. H. Mund, B. Ahuja, Mater. Res. Bull. 85, 228–233, (2017). https://doi.org/10.1016/j.materresbull.2016.09.027.
- [4]. H. Moradmard, S.F. Shayesteh, P. Tohidi, Z. Abbas, M. Khaleghi, J. Alloys Compd. 650, 116–122, (2015). https://doi.org/10.1016/j.jallcom.2015.07.269
- [5]. K. Zaharieva, V. Rives, M. Tsvetkov, Z. Cherkezova-Zheleva, B. Kunev, R.Trujillano, I. Mitov, M. Milanova, Mater. Chem. Phys. 160, (2015) 271–278, (2015) https://doi.org/10.1016/j.matchemphys.2015.04.03
- [6]. S. Anandan, T. Selvamani, G.G. Prasad, A.M. Asiri, J.J. Wu, J. Magn. Magn. Mater. 432, 437–443, (2017).. https://doi.org/10.1016/j.jmmm.2017.02.026
- [7]. X. Liu, S. An, W. Shi, Q. Yang, L. Zhang, J. Mol. Catal. Chem. 395, 243, (2014). https://doi.org/10.1016/j.molcata.2014.08.028
- [8] A.R. Bagha, M. Gharagozlou, F. Emami, J. Environ. Chem. Eng. 4, 1530, (2016). https://doi.org/10.1016/j.jece.2016.02.014
- [9]. J. Wang, Q. Deng, M. Li, K. Jiang, J. Zhang, Z. Hu, J. Chu, Sci. Rep. 7, (2017). https://doi.org/10.1038/s41598-017-09214-0
- [10]. D. Bresser, F. Mueller, M. Fiedler et al., Chemistry of Materials, vol. 25, no. 24, pp. 4977–4985, (2013). https://doi.org/10.1021/cm403443t
- [11].S. Shi, X. Zhuang, B. Cheng, and X. Wang, Journal of Materials Chemistry A, vol. 1, no. 44 pp. 13779–13788, (2013). https://doi.org/10.1039/C3TA13247A
- [12]. S. Shi, X. Zhuang, B. Cheng, and X. Wang, Journal of Materials Chemistry A, vol. 1, no. 44, pp. 13779–13788, (2013). https://doi.org/10.1039/C3TA13247A
- [13]. D. Nadhiya, A. Kala, P. Sasikumar, Mustafa K. A. Mohamm, 27(6), 101696, (2023). https://doi.org/10.1016/j.jscs.2023.101696
- [14].López-Ramón, M. V.; Álvarez, M. A.; Moreno-Castilla, C.; Fontecha-Cámara, M. A.; Yebra-Rodríguez, Á.; Bailón-García, E. J. Colloid Interface Sci. 511, 193–202, (2018). https://doi.org/10.1016/j.jcis.2017.09.117.
- [15]. Zhuravlev, V. A.; Minin, R. V.; Itin, V. I.; Lilenko, I. Y. J. Alloys Compd, 692, 705–712. 641, (2017). https://doi.org/10.1016/j.jallcom.2016.09.069.
- [16]. Amira S. Hamed, I.A. Ali, M. El Ghazaly, M. Al-Abyad, H.E. Hassan, Physica B: Condensed Matter, 607(15), 412861, (2021). https://doi.org/10.1016/j.physb.2021.412861
- [17].P. Geetha Devi A. Sakthi Velu, J Theor Appl Phys, 10:233–240, (2016). https://doi.org/10.1007/s40094-016-0221-0
- [18]. Garima Vaish, Ram Kripal, Lokendra Kumar, Journal of Material Science: Materials in Electronics, 30:16518-16526, (2019). https://doi.org/10.1007/s10854-019-02028-y
- [19]. V.RVenu Gopal, Susmita Kamila, Appl Nanosci, 7:75-82, (2017). https://doi.org/10.1007/s13204-017-0553-3
- [20]. PradeepChavan, L.R.Naik, Phys. Status Solidi (A) Applications and Materials, 214, 9,1700077, (2017). https://doi.org/10.1002/pssa.201700077
- [21]. L. Khanna, G. Gupta, S.K. Tripathi, Mater.Sci. Eng. C 97, 552–566, (2019). https://doi.org/10.1016/J.MSEC.2018.12.051.

Nanotechnology Perceptions Vol. 20 No.6 (2024)

- [22].R.S. Yadav, J. Havlica, J. Masilko, L. Kalina, J. Wasserbauer, M. Hajdúchová, V. Enev, I. Kuřitka, Z. Kožáková, J.Supercond. Nov. Magn. 29, 759–769, (2016). https://doi.org/10.1007/s10948-015-3339-4
- [23].G. Ravi Kumar, K. Vijaya Kumar, Y. Chetty Venudhar, Mater. Sci. Appl. 3, 87–91, (2012). https://doi.org/10.4236/msa.2012.32013.
- [24]. Wahba, A.M., Moharam, B.E.M. & Mahmoud, A.F. J.Mater.Sci: Mater Electron, 32, 14194-14206, (2021). https://doi.org/10.1007/s10854-021-05978-4.
- [25]. Adel Maher Wahaba, Bahaa Eldeen M, Moharam, Aya Fayez Mamoud, 32,14194-14206, (2021). https://doi.org/10.1007/s10854-021-05978-4.
- [26]. Ninad B. Velhal; Narayan D. Patil; Abhijeet R. Shelke; Nishad G. Deshpande; Vijaya R. Puri, 5, 097166, (2015). https://doi.org/10.1063/1.4931908
- [27]. FatenHaithumMulud 1, Najat A.Dahham 1, Ibrahim F. Waheed, 928, 072125, (2020). https://dx.doi.org/10.1088/1757-899X/928/7/072125
- [28]. N. Ponpandian, P. Balaya, A. Narayanasamy, J. Phys. 14, 3221–3237, (2021). https://doi.org/10.1088/0953-8984/14/12/311
- [29]. Schwartz, V. B., Thétiot, F., Ritz, S., Pütz, S., Choritz, L., Lappas, A., et al. 22, 2376–2386, (2012). https://doi.org/10.1002/adfm.201102980